Distinct role of electric field and vector potential in strong-field tunneling ionization

Yongzhe Ma,[1,2,*] Xiaodan Mao,[2,*] Lanhe Kong,[2,3] Qingcao Liu,[1] Hongcheng Ni,[2,4,†] and Jian Wu[2,4,5]

[1]*College of Science, Harbin Institute of Technology, Weihai, Shandong 264209, China*

[2]*State Key Laboratory of Precision Spectroscopy, East China Normal University, Shanghai 200241, China*

[3]*School of Physics and Electronic Science, East China Normal University, Shanghai 200241, China*

[4]*Collaborative Innovation Center of Extreme Optics, Shanxi University, Taiyuan, Shanxi 030006, China*

[5]*Chongqing Key Laboratory of Precision Optics, Chongqing Institute of East China Normal University, Chongqing 401121, China*

(Received 15 November 2024; accepted 21 February 2025; published 6 March 2025)

Light can be described either by its field or potential, which are often interchangeable. We theoretically investigate the distinct roles of the electric field and the vector potential of an ultrashort laser pulse in strong-field tunneling ionization, based on their distinct central frequencies. Employing the conservation law between the angular momentum and energy, we demonstrate that quantum tunneling dynamics is driven by the electric field, while the subsequent classical motion in the continuum is governed by the vector potential. Our work casts new light on the fundamental laser-matter interactions and offers a fresh perspective on the application of ultrashort laser pulses in strong-field physics.

DOI: 10.1103/PhysRevA.111.033103

I. INTRODUCTION

An electromagnetic wave can be represented either by its electric and magnetic fields or, alternatively, by scalar and vector potentials. While the field and potential descriptions are generally considered equivalent in classical electromagnetism, the Aharonov-Bohm effect suggests that the potential representation can be seen as being more fundamental. Recently, this interpretation has been challenged that the Aharonov-Bohm effect can be explained without relying on vector potentials [1–4]. Laser-matter interaction stands as a unique ground where respective roles of the field and potential can be studied. In particular, for a laser pulse propagating in vacuum, the scalar potential vanishes, and within the dipole approximation, the magnetic field can be ignored. In this respect, the question reduces to whether laser-matter interaction is better described by the electric field or the vector potential.

With the advent of ultrashort laser pulses, the study of laser-matter interaction has progressed to a new realm. Benefiting from their unique properties, such as high peak intensity and high temporal precision, ultrashort laser pulses with only a few oscillation periods hold tremendous potential for applications in strong-field physics. For instance, using ultrashort laser pulses enables the ultrafast resolution of electron dynamics in atoms and molecules [5–7] and the extraction of atomic and molecular structural information [8,9], as well as the control of light-induced chemical reactions [10–13]. For an ultrashort few-cycle pulse, the carrier-envelope phase is a unique tunable parameter to control the pulse shape, thereby steering electron dynamics in atoms and molecules [14,15].

In addition to the carrier-envelope phase, the carrier frequency of laser pulses is also an important characteristic parameter. Unlike long laser pulses, ultrashort pulses exhibit a significant difference in the carrier frequencies of their electric field and vector potential, which may influence quantum excitation and ionization processes [16,17]. This property of ultrashort pulses renders them an excellent platform for studying the distinct roles of the electric field and vector potential in light-matter interactions.

In this article, we focus on the role of electric field and vector potential in strong-field tunneling ionization, a two-stage process including an underbarrier quantum tunneling and a subsequent classical continuum motion. Making use of the conservation law between the angular momentum and energy [18,19], we demonstrate that the characteristics of photoelectrons at the tunnel exit are related to the carrier frequency of the electric field, indicating that quantum tunneling is governed by the electric field. Conversely, the dynamic information of photoelectrons in the asymptotic region is linked to the carrier frequency of the vector potential, suggesting that the classical continuum motion is ruled by the vector potential. We note that our conclusions are independent of the dimensionality of the model and the specific form of the potential. For simplicity, we restrict our discussions to two dimensions using a short-range potential.

This article is organized as follows. In Sec. II, we detail the ultrashort laser pulse used in our study. In Sec. III, we depict the two-step process of tunneling ionization. In Sec. IV, we focus on the underbarrier tunneling process, where we show that its dynamics is driven by the electric field. In Sec. V, we move on to the subsequent continuum motion; we demonstrate that it is governed by the vector potential. In Sec. VI, we discuss the generality of our findings. In Sec. VII, we discuss the physical origin of our findings. Conclusions are given in Sec. VIII. Atomic units are used throughout unless specified otherwise.

*These authors contributed equally to this work.

†Contact author: hcni@lps.ecnu.edu.cn

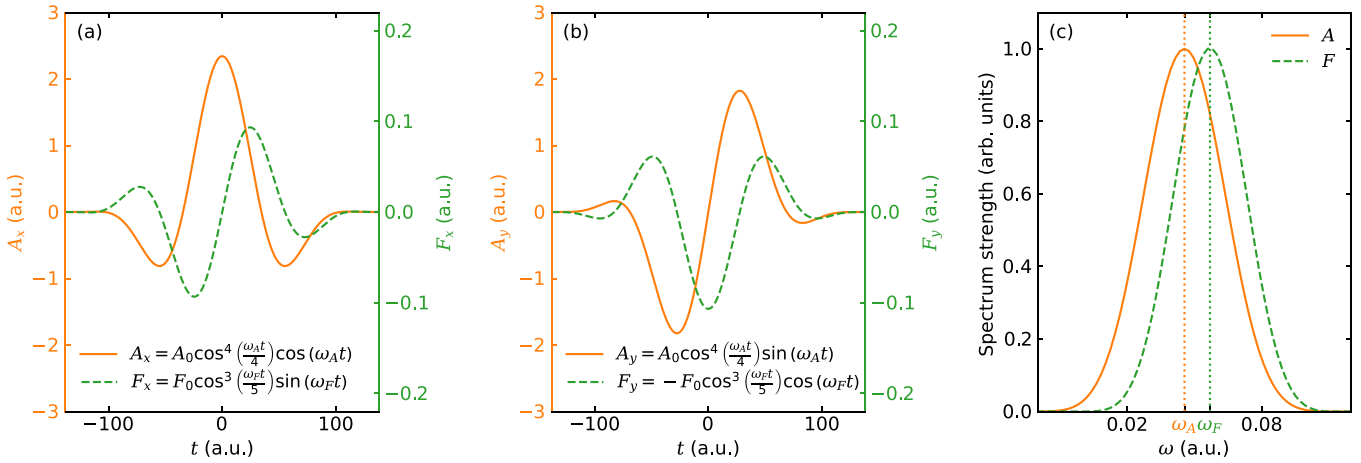

FIG. 1. Sketch of the (a) x component and (b) y component of the vector potential (orange solid line) and electric field (green dashed line) for the present circularly polarized laser pulse. (c) The frequency spectrum of the electric field and vector potential. The carrier frequency of the vector potential is $\omega_A = 0.04556$ a.u., corresponding to a wavelength of 1000 nm, and that of the electric field is $\omega_F = \frac{5}{4}\omega_A = 0.05695$ a.u., corresponding to a wavelength of 800 nm.

II. ULTRASHORT LASER PULSE

To elucidate the findings, we first introduce ultrashort laser pulses, where the vector potential can be expressed as the product of the carrier wave and an envelope function. Under the dipole approximation, the vector potential of an ultrashort circularly polarized laser pulse can be defined in the x-y polarization plane as

$$\boldsymbol{A}(t) = A_0 \cos^4\left(\frac{\omega_A t}{4}\right)[\cos(\omega_A t)\hat{\boldsymbol{e}}_x + \sin(\omega_A t)\hat{\boldsymbol{e}}_y], \qquad (1)$$

where A_0 is the amplitude of the vector potential corresponding to a laser intensity of 8×10^{14} W/cm^2, ω_A is the carrier frequency of the vector potential corresponding to a wavelength of 1000 nm, and the total pulse duration involves two cycles. The Keldysh parameter is $\gamma = 0.57$, indicating ionization in the tunneling regime. The corresponding electric field $\boldsymbol{F}(t) = -\dot{\boldsymbol{A}}(t)$ is

$$\begin{aligned}\boldsymbol{F}(t) &= F_0 \cos^3\left(\frac{\omega_A t}{4}\right)\left[\sin\left(\frac{5}{4}\omega_A t\right)\hat{\boldsymbol{e}}_x - \cos\left(\frac{5}{4}\omega_A t\right)\hat{\boldsymbol{e}}_y\right] \\ &= F_0 \cos^3\left(\frac{\omega_F t}{5}\right)[\sin(\omega_F t)\hat{\boldsymbol{e}}_x - \cos(\omega_F t)\hat{\boldsymbol{e}}_y], \qquad (2)\end{aligned}$$

where $F_0 = A_0\omega_A$ is the amplitude of the electric field and $\omega_F = \frac{5}{4}\omega_A$ is the carrier frequency of the electric field corresponding to a wavelength of 800 nm.

We select this specific form for the ultrashort laser pulse for two primary reasons. First, by defining the laser pulse through the vector potential $\boldsymbol{A}(t)$, we ensure that it vanishes at the pulse conclusion. Second, this form allows the electric field to be expressed as the product of an envelope function and a monochromatic carrier wave, similar to the vector potential. The benefits of this approach are clear: the carrier frequencies associated with the electric field and the vector potential can be clearly differentiated and maintain a specific relationship. Under the modulation of the envelope function, the vector potential completes two oscillations within the pulse duration, whereas the electric field completes 2.5 oscillations. Consequently, the central frequency of the electric field is $\frac{5}{4}$ times that of the vector potential, as illustrated in Fig. 1. These distinctive properties will be manifested in measurable physical quantities, thereby providing a foundation for discerning the separate contributions of the electric field and vector potential to tunneling ionization.

III. TWO-STEP TUNNELING IONIZATION

Tunneling ionization of atoms and molecules upon interaction with intense lasers is the basis of many strong-field phenomena, which can be divided into two steps: the quantum tunneling process of the electron under the potential barrier and the subsequent classical motion of the electron in the continuum, as sketched in Fig. 2. The information of these two processes will be imprinted on the tunneling exit characteristics and asymptotic photoelectron momentum distribution (PMD), respectively.

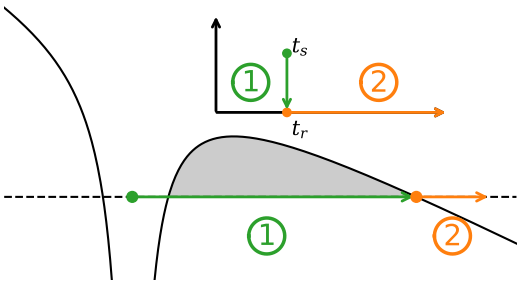

FIG. 2. Schematic diagram of the tunneling ionization process. It is divided into two steps. The first step is quantum tunneling, that is, the laser field bends the Coulomb potential to form a potential barrier and the electron moves under the potential barrier from the saddle-point time t_s to the ionization time t_r, as shown by the green arrow. The second step is the classical motion of the electron starting from the ionization time t_r, indicated by the orange arrow.

In order to accurately obtain the PMD, we numerically solve the time-dependent Schrödinger equation (TDSE)

$$i\frac{\partial}{\partial t}\psi(\boldsymbol{r},t)=\left\{\frac{1}{2}[\hat{\boldsymbol{p}}+\boldsymbol{A}(t)]^2+V(r)\right\}\psi(\boldsymbol{r},t), \tag{3}$$

where $\hat{\boldsymbol{p}}$ is the momentum operator. For the purpose of excluding the influence of the long-range Coulomb potential on the asymptotic momentum, a short-range potential is used,

$$V(r)=-(e^{-100r}+e^{-r^2/2})/\sqrt{r^2+a}, \tag{4}$$

where $a=0.01745$ is the soft-core parameter tuned to match the ionization potential of the helium atom. The TDSE simulation is carried out on a two-dimensional grid with a grid step of $\Delta x=0.2$ a.u. and 2048 grid points in each direction, and a time step of $\Delta t=0.02$ a.u. The ground-state wave function is obtained by the imaginary-time propagation method and the evolution of the wave function in the laser field is carried out using the split-operator Fourier method. An absorber of the form $1/[1+\exp\{(r-r_0)/d\}]$, where $r_0=189.8$ and $d=4$ a.u., is placed around the center of the simulation box to damp the outgoing wave packet in order to avoid reflections from the grid border.

The asymptotic momentum distribution is obtained by accumulatively projecting the absorbed wave function onto the Volkov state at each time step [20,21]. In addition, we employ the backpropagation method [7,22–26] to extract the tunneling exit characteristics, which includes three steps: the electron wave function is first evolved quantum mechanically by solving the TDSE, then the quantum flux passing through the virtual detectors [27–30] placed around the atom are converted into classical trajectories, and finally the classical trajectories are backpropagated along the time axis until a tunneling criterion [24] is satisfied. This hybrid quantum-classical approach has been widely used in various studies, such as exploring the subcycle linear momentum transfer [31], probing backscattering time [32], reconciling conflicts in tunneling time delay [33], and investigating the tunneling dynamics of atomic p orbitals [34–36], as a proven effective method to obtain tunneling exit information.

IV. UNDERBARRIER QUANTUM TUNNELING

The correlated spectrum of angular momentum and energy (SAME) [18] is a valuable tool for evaluating the properties of photoelectrons, which is promising towards distinguishing the contribution of the electric field and vector potential of ultrashort laser pulses to tunneling ionization processes.

We begin by examining the properties of photoelectrons at the tunnel exit. As depicted in Fig. 3(a), the SAME for photoelectrons at the tunnel exit upon interaction with the ultrashort circularly polarized laser pulse is reconstructed using backpropagation. Remarkably, the SAME exhibits a narrow linear distribution, leading to the conservation law [18,19]

$$E=\omega L_z-I_p, \tag{5}$$

with ω the slope of the SAME and I_p the ionization potential. For the present ultrashort laser pulse, the SAME of the photoelectron at the tunnel exit has a slope $\omega=\omega_F$ in Fig. 3(a). This indicates that the characteristics of photoelectrons at the tunnel exit are determined by the carrier frequency of the electric field. It should be noted that the SAME retrieved from backpropagation exhibits a slight downward shift and curvature with respect to Eq. (5) due to the attractive potential of the parent ion [18].

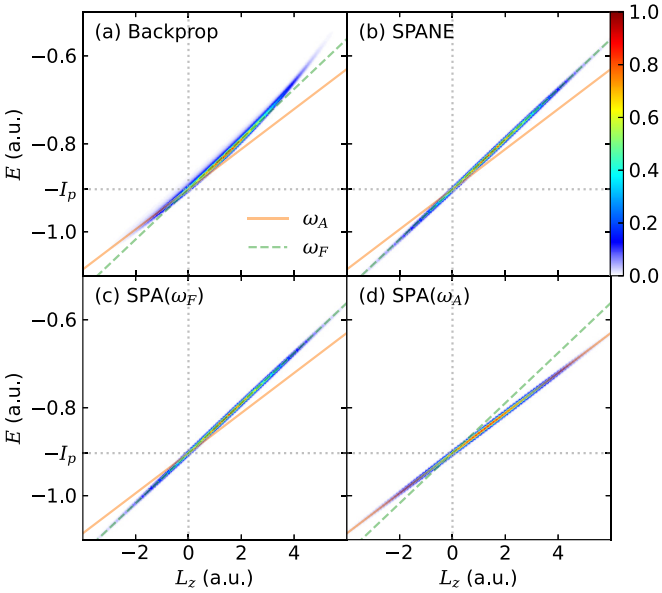

FIG. 3. Correlated spectra of angular momentum and energy (SAME) of photoelectrons at the tunnel exit under the interaction with the ultrashort laser pulse obtained by (a) backpropagation and (b) SPANE. The SAME obtained by the SPA method for infinitely long circularly polarized laser pulses for (c) $\omega=\omega_F$ and (d) $\omega=\omega_A$. The orange solid lines denote $E=\omega_A L_z-I_p$ and the green dashed lines denote $E=\omega_F L_z-I_p$.

In order to gain a deeper understanding of this behavior, we employ the saddle-point approximate with nonadiabatic expansion (SPANE) [7,24,37–40] within the framework of strong-field approximation (SFA) [41,42] to obtain the SAME for the ultrashort laser pulse, as shown in Fig. 3(b). Within this framework, the relationship between the energy and angular momentum of the photoelectron at the tunnel exit can be derived analytically, giving

$$E=\omega_F L_z-I_p, \tag{6}$$

where the frequency of the electric field ω_F comes into play instead of that of the vector potential ω_A. Theoretical details are given in Appendix B. This suggests that the quantum tunneling dynamics is driven by the electric field, not the vector potential.

For an infinitely long laser pulse, the frequencies of the electric field and the vector potential are identical, which we denote as ω. We employ the saddle-point approximation (SPA) [43,44] to obtain the SAME under infinitely long laser pulses with frequencies $\omega=\omega_F$ and $\omega=\omega_A$, as shown in Figs. 3(c) and 3(d), respectively. It is evident that, when the frequency $\omega=\omega_F$ is applied in SPA, the SAME [Fig. 3(c)] aligns with that obtained by backpropagation [Fig. 3(a)], which further strengthens the notion that it is the electric field that drives the quantum tunneling dynamics.

The transverse momentum distribution at the tunnel exit is a recognized indicator of nonadiabaticity during tunneling,

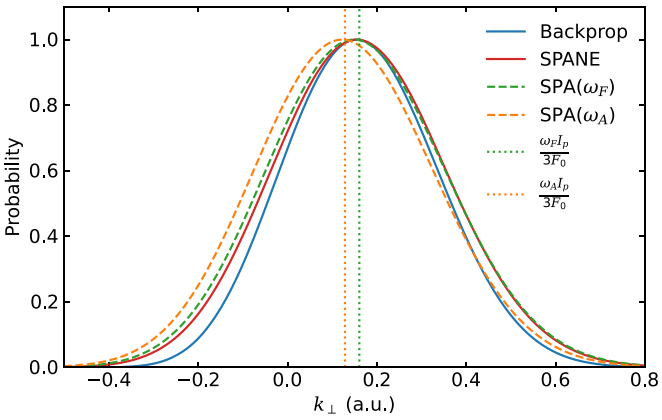

FIG. 4. Transverse momentum distribution at the tunnel exit. The blue solid line is obtained by backpropagation, the red solid line is obtained by SPANE, and the green and orange dashed lines are obtained by the SPA method, with frequencies ω_F and ω_A, respectively. The green and orange dotted lines represent the peak transverse momentum corresponding to the frequencies ω_F and ω_A, respectively.

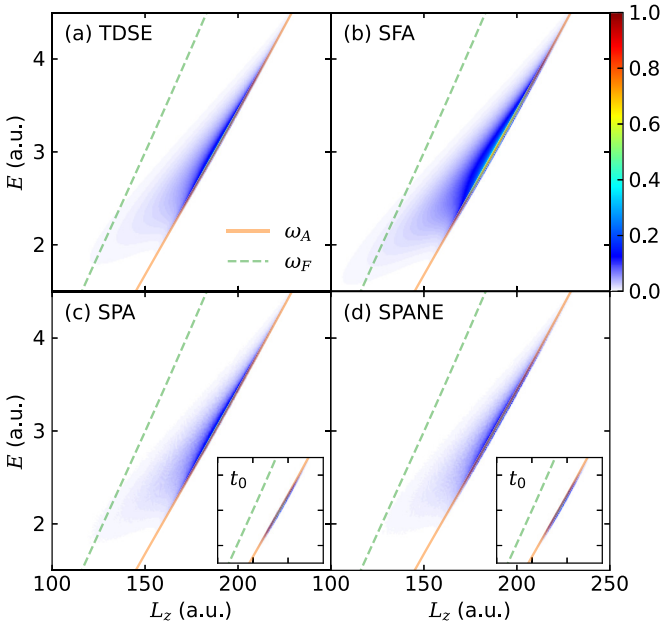

FIG. 5. Correlated spectra of angular momentum and energy (SAME) of photoelectrons after the interaction with the ultrashort laser pulse obtained by (a) TDSE, (b) SFA, (c) SPA, and (d) SPANE. The insets in the lower row illustrate the SAME at the pulse center ($t = t_0$). The orange solid lines denote Eq. (7), whereas the green dashed lines represent Eq. (7) where ω_A is replaced with ω_F.

which in turn depends on the laser frequency and thus can also be used to discern the contributions of the electric field and vector potential to the tunneling process. Figure 4 illustrates such a transverse momentum distribution. As anticipated, the distribution varies under infinitely long circularly polarized laser pulses of different frequencies. A higher laser frequency results in a larger Keldysh parameter, which in turn enhances the nonadiabatic effect, resulting in a greater offset of the transverse momentum distribution from zero. Specifically, the distribution for $\omega = \omega_F$ (green dashed line) shifts to the right compared to that for $\omega = \omega_A$ (orange dashed line), as obtained from the SPA. This offset lays the basis for identifying the frequency contributions of ultrashort pulses to physical processes. In the context of ultrashort circularly polarized laser pulses, the peak of the transverse momentum distribution of photoelectrons, as determined by backpropagation (blue solid line) and SPANE (red solid line), is located near $\frac{\omega_F I_p}{3F_0}$ (green dotted line) [Eq. (B12)]. It demonstrates that the transverse momentum distribution of photoelectrons at the tunnel exit is associated with the electric-field frequency of the ultrashort laser pulse, thereby reaffirming that quantum tunneling dynamics is governed by the electric field.

V. CLASSICAL CONTINUUM MOTION

Now we turn to the asymptotic PMD, from which we identify the contribution of the electric field and vector potential to the second step of tunneling ionization, i.e., the classical continuum motion. Figure 5 presents the SAME in the asymptotic region calculated using (a) TDSE, (b) SFA, (c) SPA, and (d) SPANE after the conclusion of the ultrashort laser pulse. In contrast to the simple conservation law between the angular momentum and energy at the tunnel exit [Eq. (5)], their relation in the asymptotic region is more complicated:

$$L_z = \frac{1}{\omega_A}\left[\frac{4}{5-\sqrt{U_p/E}}(I_p + E_0) + \frac{4}{3}(U_p + E - E_0)\right], \quad (7)$$

where $E_0 = E(1-\sqrt{U_p/E})^2$ is the initial energy at the tunnel exit and $U_p = A_0^2/2$ is the ponderomotive energy. Theoretical details are given in Appendix B. It is clear from Fig. 5 that the SAME derived from all methods closely follows Eq. (7) (orange solid lines), with the frequency corresponding to the vector potential ω_A. Conversely, using the frequency of the electric field ω_F leads to significant discrepancies (green dashed lines). This indicates that the information carried by the photoelectrons in the asymptotic region is determined by the frequency of the vector potential. We note that the broadened distribution of the SAME is attributed to varying laser amplitude at different time instances. As illustrated in the insets of panels (c) and (d), the SAME, when sliced at the pulse peak ($t = t_0$), aligns perfectly with the orange solid lines given by Eq. (7).

In addition, we shown in Fig. 6 the asymptotic PMD obtained from TDSE sliced at the maximum emission angle $\theta_{\max}$ (blue solid line) and that from SPANE sliced at the pulse center t_0 (red solid line), which agree well with each other. They also correspond well with the results obtained with long pulses from SPA using the frequency of the vector potential ω_A (orange dashed line) rather than that of the electric field ω_F (green dashed line). In addition, the peak position in the PMD can be divided into two components, corresponding to the two stages of tunneling ionization. The first component is the initial transverse momentum, determined by the carrier frequency of the electric field $\frac{\omega_F I_p}{3F_0}$, and the second component is the vector potential corresponding to a frequency of ω_A. These observations suggest that the classical continuum motion is ruled by the vector potential.

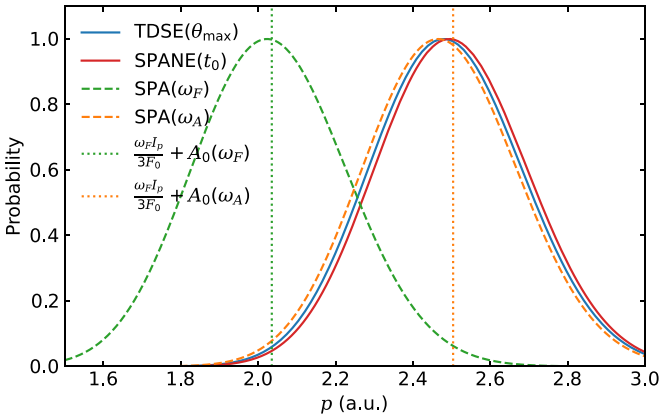

FIG. 6. Asymptotic photoelectron momentum distribution. The blue solid line is obtained by TDSE sliced at the maximum emission angle θ_{max}, the red solid line is obtained by SPANE sliced at the pulse center t_0, and the green and orange dashed lines are obtained by SPA for long pulses with frequencies ω_F and ω_A, respectively. The green and orange dotted lines represent the sum of the average initial transverse momentum $\frac{\omega_F I_p}{3F_0}$ and the vector potential corresponding to the frequencies ω_F and ω_A, respectively.

VI. GENERALITY

It is important to note that our findings are general and not limited to specific laser parameters. To verify this, we present the SAME at different laser intensities and wavelengths in Figs. 7 and 8, for the tunnel exit and asymptotic region, respectively. The results were obtained using the SPANE method and we have verified that the time-dependent Schrödinger equation or backpropagation leads to the same conclusions, although the corresponding figures are omitted for brevity.

At the tunnel exit, the relation $E = \omega_F L_z - I_p$ [Eq. (6)] the SAME follows remains unchanged with varying intensity when the wavelength is kept fixed [Fig. 7(a)], confirming that tunneling dynamics are governed by the electric field. When the wavelength is varied at fixed intensity, the slope of the SAME changes, but the relationship between angular momentum and energy is preserved [Fig. 7(b)]. This shows that our conclusions are independent of the Keldysh parameter.

In the asymptotic region, similarly, the slope of the SAME is consistently determined by the frequency of the vector potential, regardless of variations in intensity, wavelength, or the Keldysh parameter (Fig. 8). This illustrates that the continuum motion of the photoelectrons after tunneling is governed by the vector potential and further supports the universality of our findings.

Additionally, we have verified that our conclusions are gauge invariant for both TDSE and SPANE calculations, implying that one cannot directly infer the effects of the electric field or vector potential on photoelectron dynamics from the interaction terms. See Appendix C for details.

Furthermore, our conclusions are independent of the dimensionality of the model used. As shown in Appendix D, the present findings hold valid for three-dimensional models as well.

VII. DISCUSSIONS

Our insights into the roles of the electric field and vector potential in tunneling ionization can be explained with straightforward physical reasoning. For the classical continuum motion, the asymptotic momentum can be expressed as

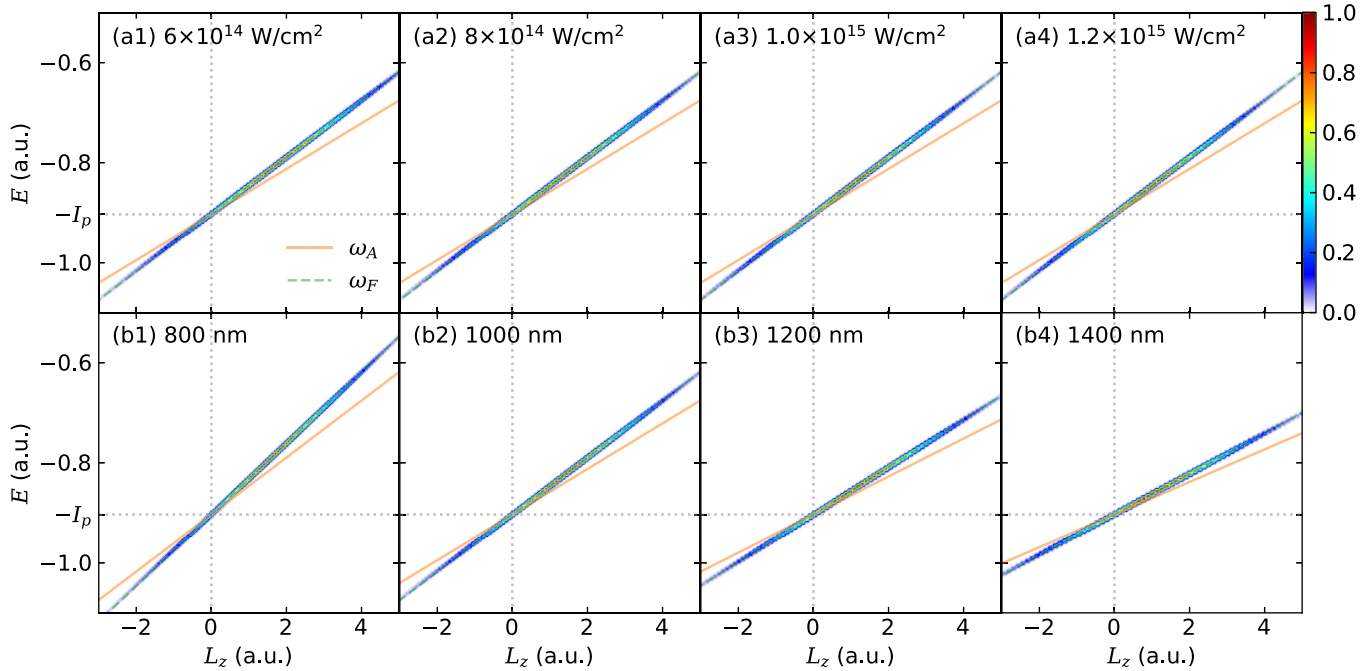

FIG. 7. Correlated spectra of angular momentum and energy (SAME) of photoelectrons at the tunnel exit under the interaction with the ultrashort laser pulse of different parameters. In row (a), the wavelength of the vector potential is held constant at 1000 nm, while the peak intensity is varied. In row (b), the peak intensity is kept constant at 8×10^{14} W/cm^2, while the wavelength of the vector potential is varied.

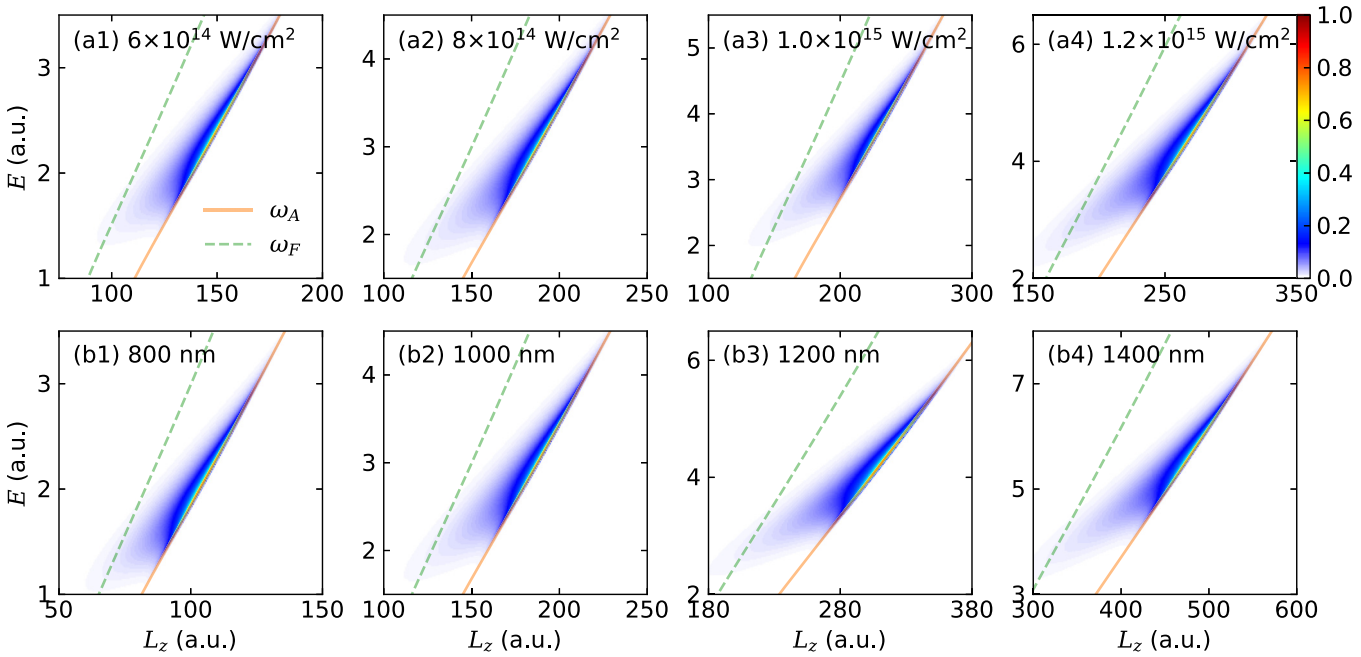

FIG. 8. Correlated spectra of angular momentum and energy (SAME) of photoelectrons in the asymptotic region under the interaction with the ultrashort laser pulse of different parameters. In row (a), the wavelength of the vector potential is held constant at 1000 nm, while the peak intensity is varied. In row (b), the peak intensity is kept constant at 8×10^{14} W/cm^2, while the wavelength of the vector potential is varied.

$\boldsymbol{p} = \boldsymbol{k}_\perp - \int_{t_r}^{\infty} \boldsymbol{F}(t)dt = \boldsymbol{k}_\perp - \boldsymbol{A}(t_r)$, where $\boldsymbol{k}_\perp$ represents the initial momentum at the tunnel exit, which is typically very small. Since the integration of the electric field is performed over real time (as depicted in Fig. 2), this results in the vector potential. Consequently, the asymptotic momentum is connected to the vector potential. In contrast, during the quantum tunneling phase, only imaginary time elapses (as shown in Fig. 2) and it is the electric field that remains the dominant factor.

Remarkably, the frequency ratio of $\frac{\omega_F}{\omega_A} = \frac{5}{4}$ is essentially the maximal achievable ratio in our present study. This is because the total optical cycle $N = 2$ corresponds to a single-cycle pulse when measured at its full width at half maximum, where the distinction of the electric field and vector potential is optimal. Furthermore, it is worth noting that the conservation law between angular momentum and energy has been proposed for experimental verification using electron vortices [18]. Therefore, our findings could be experimentally validated by monitoring the slope of the asymptotic SAME as the pulse duration is varied. In addition, the SAME at the tunnel exit can be inferred from that in the asymptotic region by accounting for the energy and photon absorption during the continuum motion [18].

VIII. CONCLUSION

In conclusion, our study has elucidated the distinct roles of the electric field and vector potential in strong-field tunneling ionization. By employing ultrashort laser pulses, where the carrier frequencies of the electric field and the vector potential differ, we have been able to differentiate their individual contributions. Leveraging the conservation law between angular momentum and energy, we have demonstrated that quantum tunneling is driven by the electric field, while the subsequent classical motion in the continuum is directed by the vector potential. Our findings shed new light on the fundamental interactions between light and matter, providing a novel perspective on the utilization of ultrashort laser pulses in the realm of strong-field physics.

ACKNOWLEDGMENTS

This work was supported by the National Natural Science Foundation of China (Grants No. 92150105, No. 12474341, No. 12227807, No. 12241407, and No. 12034020), the Science and Technology Commission of Shanghai Municipality (Grant No. 23JC1402000), the Shanghai Pilot Program for Basic Research (Grant No. TQ20240204), and the Science Foundation of Shandong Province (Grant No. 2022HWYQ-073). Numerical computations were in part performed on the ECNU Multifunctional Platform for Innovation (001).

APPENDIX A: SADDLE-POINT APPROXIMATION FOR LONG PULSES

According to the strong-field approximation (SFA) in the length gauge [41,42], the transition amplitude between an atomic bound state and the continuum state with photoelectron asymptotic momentum $\boldsymbol{p}$ is given by

$$M_{\boldsymbol{p}}^{\mathrm{SFA}} = -i \int_{-\infty}^{+\infty} \langle \psi_{\boldsymbol{p}}(\boldsymbol{r}, t) | \boldsymbol{r} \cdot \boldsymbol{F}(t) | \psi_0(\boldsymbol{r}, t) \rangle dt, \qquad \text{(A1)}$$

where $\psi_0(\boldsymbol{r}, t) = \psi_0(\boldsymbol{r}) e^{iI_p t}$ is the initial bound-state wave function unperturbed by the laser field with I_p standing for

the ionization potential and

$$\psi_{\boldsymbol{p}}(\boldsymbol{r},t)=\exp\left\{i[\boldsymbol{p}+\boldsymbol{A}(t)]\cdot\boldsymbol{r}-\frac{i}{2}\int^{t}[\boldsymbol{p}+\boldsymbol{A}(t')]^2dt'\right\} \tag{A2}$$

is the Volkov state. Through the application of saddle-point approximation (SPA), the transition amplitude is obtained by [43,44]

$$M_{\boldsymbol{p}}^{\mathrm{SPA}}=\sum_{t_s}\frac{\exp(iS_s)}{\{[\boldsymbol{p}+\boldsymbol{A}(t_s)]\cdot\boldsymbol{F}(t_s)\}^{\alpha/2}}, \tag{A3}$$

with the phase

$$S_s=-\int_{t_s}^{t_r}\left\{\frac{1}{2}[\boldsymbol{p}+\boldsymbol{A}(t)]^2+I_p\right\}dt, \tag{A4}$$

and $\alpha=1+Z/\sqrt{2I_p}$ with $Z=1$ the asymptotic charge. The saddle-point times t_s are identified according to the saddle-point equation

$$\tfrac{1}{2}[\boldsymbol{p}+\boldsymbol{A}(t_s)]^2+I_p=0, \tag{A5}$$

where $t_s=t_r+it_i$ must be a complex number to satisfy the saddle-point equation, with t_r the tunneling exit time and t_i relating to the ionization probability.

Rearranging Eq. (A5) gives its imaginary part

$$i\boldsymbol{k}_\perp\cdot\mathrm{Im}\boldsymbol{A}(t_s)=0, \tag{A6}$$

where $\boldsymbol{k}_\perp=\boldsymbol{p}+\mathrm{Re}\boldsymbol{A}(t_s)$. By defining the auxiliary momentum $k_\perp$ as

$$k_\perp=\frac{-\mathrm{Im}A_y(t_s)\hat{\boldsymbol{e}}_x+\mathrm{Im}A_x(t_s)\hat{\boldsymbol{e}}_y}{\sqrt{[\mathrm{Im}A_x(t_s)]^2+[\mathrm{Im}A_y(t_s)]^2}}\boldsymbol{k}_\perp, \tag{A7}$$

the imaginary part of the saddle-point equation [Eq. (A6)] is fulfilled automatically. In the $(t_r,\ k_\perp)$ coordinate system, it suffices to find the solution to the real part of the saddle-point equation, leading to a substantial increase in computational efficiency compared to searching for the complex saddle-point times across the full complex plane. Furthermore, when calculating the ionization rate, the Jacobian factor of coordinate transformation needs to be taken into account.

For an infinitely long circularly polarized laser pulse, the carrier frequency of the electric field and the vector potential are identical. So the vector potential can be defined as

$$\boldsymbol{A}(t)=A_0[\cos(\omega t)\hat{\boldsymbol{e}}_x+\sin(\omega t)\hat{\boldsymbol{e}}_y] \tag{A8}$$

and the corresponding electric field $\boldsymbol{F}(t)=-\dot{\boldsymbol{A}}(t)$ is

$$\boldsymbol{F}(t)=F_0[\sin(\omega t)\hat{\boldsymbol{e}}_x-\cos(\omega t)\hat{\boldsymbol{e}}_y]. \tag{A9}$$

Solving Eq. (A5) results in

$$t_r=\frac{1}{\omega}\left[\arctan\left(\frac{p_y}{p_x}\right)+\pi\right], \tag{A10}$$

$$t_i=\frac{1}{\omega}\mathrm{arccosh}\left(\frac{E+I_p+U_p}{A_0p}\right), \tag{A11}$$

where the energy $E=p^2/2$, the asymptotic momentum $p=\sqrt{p_x^2+p_y^2}$, and the ponderomotive energy $U_p=A_0^2/2$. Thus the transition probability, up to exponential precision, is

$$\begin{aligned}W_{\mathrm{SPA}}&=\exp\{-2\,\mathrm{Im}S_s\}\\&=\exp\left\{2\frac{E+I_p+U_p}{\omega}\left[\left(1-\frac{A_0^2p^2}{(E+I_p+U_p)^2}\right)^{\frac{1}{2}}\right.\right.\\&\quad\left.\left.-\mathrm{arccosh}\left(\frac{E+I_p+U_p}{A_0p}\right)\right]\right\}.\end{aligned} \tag{A12}$$

The information of photoelectrons at the tunnel exit can be extracted through the SPA method. The tunneling exit position is given as

$$\begin{aligned}\boldsymbol{r}_0&=\mathrm{Re}\int_{t_s}^{t_r}[\boldsymbol{p}+\boldsymbol{A}(t)]dt=\mathrm{Im}\int_0^{t_i}\boldsymbol{A}(t_r+it)dt\\&=\frac{E+I_p+U_p-A_0p}{\omega p^2}(p_y\hat{\boldsymbol{e}}_x-p_x\hat{\boldsymbol{e}}_y)\end{aligned} \tag{A13}$$

and the initial momentum at the tunnel exit is

$$\boldsymbol{k}_\perp=\boldsymbol{p}+\boldsymbol{A}(t_r)=\left(1-\frac{A_0}{p}\right)\boldsymbol{p}. \tag{A14}$$

Therefore, the angular momentum at the tunnel exit is subsequently obtained by

$$\boldsymbol{L}=\boldsymbol{r}_0\times\boldsymbol{k}_\perp=\left(1-\frac{A_0}{p}\right)\frac{E+I_p+U_p-A_0p}{\omega}\hat{\boldsymbol{e}}_z \tag{A15}$$

and the energy at the tunnel exit is

$$\begin{aligned}E&=\frac{1}{2}k_\perp^2+\boldsymbol{r}_0\cdot\boldsymbol{F}(t_r)=\left(1-\frac{A_0}{p}\right)(E+U_p-A_0p)-\frac{A_0I_p}{p}\\&=\omega L_z-I_p,\end{aligned} \tag{A16}$$

i.e., the conservation law of the angular momentum and energy at the tunnel exit.

APPENDIX B: SADDLE-POINT APPROXIMATE WITH NONADIABATIC EXPANSION FOR SHORT PULSES

In order to intuitively obtain the observable information of photoelectrons in the case of ultrashort laser pulses, we use saddle-point approximation with nonadiabatic expansion (SPANE) [7,24,37–40] and expand the vector potential $\boldsymbol{A}(t_s)$ in terms of small t_i (or small Keldysh parameter γ corresponding to the tunneling scenario) up to the second order,

$$\boldsymbol{A}(t_r+it_i)=\boldsymbol{A}(t_r)-it_i\boldsymbol{F}(t_r)+\tfrac{1}{2}t_i^2\dot{\boldsymbol{F}}(t_r)+O\left(t_i^3\right), \tag{B1}$$

where $\dot{\boldsymbol{F}}(t_r)=\frac{d\boldsymbol{F}(t_r)}{dt_r}$. Inserting Eq. (B1) into the saddle-point equation [Eq. (A5)], we can get

$$\boldsymbol{k}_\perp(t_r)\cdot\boldsymbol{F}(t_r)=0, \tag{B2}$$

$$t_i=\sqrt{\frac{k_\perp^2(t_r)+2I_p}{F^2(t_r)-\boldsymbol{k}_\perp(t_r)\cdot\dot{\boldsymbol{F}}(t_r)}}, \tag{B3}$$

where $F(t_r)=\sqrt{F_x^2(t_r)+F_y^2(t_r)}$ is the instantaneous electric-field magnitude and $\boldsymbol{k}_\perp(t_r)=\boldsymbol{p}+\boldsymbol{A}(t_r)$ is the initial transverse momentum at the tunnel exit. Since $\boldsymbol{k}_\perp\cdot\boldsymbol{F}(t_r)=0$

[Eq. (B2)], we define

$$k_\perp = \boldsymbol{k}_\perp \cdot \frac{F_y(t_r)\hat{\boldsymbol{e}}_x - F_x(t_r)\hat{\boldsymbol{e}}_y}{F(t_r)} \tag{B4}$$

to ensure that the imaginary part of the saddle-point equation is always satisfied.

Thereby, the imaginary part of the phase S_s

$$\begin{aligned}\mathrm{Im}S_s &= I_p t_i + \frac{1}{2}\mathrm{Re}\int_0^{t_i}[\boldsymbol{p}+\boldsymbol{A}(t_r+it)]^2 dt \\ &\approx \frac{(k_\perp^2+2I_p)^{3/2}}{3\sqrt{F^2(t_r)-\boldsymbol{k}_\perp\cdot\dot{\boldsymbol{F}}(t_r)}},\end{aligned} \tag{B5}$$

leading to the tunneling ionization probability (exponential precision)

$$\begin{aligned}W_{\mathrm{SPANE}} &= \exp\{-2\,\mathrm{Im}S_s\} \\ &= \exp\left\{-\frac{2(k_\perp^2+2I_p)^{3/2}}{3\sqrt{F^2(t_r)-\boldsymbol{k}_\perp\cdot\dot{\boldsymbol{F}}(t_r)}}\right\},\end{aligned} \tag{B6}$$

the tunneling exit position

$$\begin{aligned}\boldsymbol{r}_0 &= \mathrm{Re}\int_{t_s}^{t_r}[\boldsymbol{p}+\boldsymbol{A}(t)]dt = \mathrm{Im}\int_0^{t_i}\boldsymbol{A}(t_r+it)dt \\ &= -\frac{\boldsymbol{F}}{2}\frac{k_\perp^2+2I_p}{F^2-\boldsymbol{k}_\perp\cdot\dot{\boldsymbol{F}}},\end{aligned} \tag{B7}$$

the angular momentum at the tunnel exit

$$\boldsymbol{L} = \boldsymbol{r}_0\times\boldsymbol{k}_\perp = \frac{Fk_\perp(k_\perp^2+2I_p)}{2(F^2-\boldsymbol{k}_\perp\cdot\dot{\boldsymbol{F}})}\hat{\boldsymbol{e}}_z, \tag{B8}$$

and the energy at the tunnel exit

$$\begin{aligned}E &= \frac{1}{2}k_\perp^2 + \boldsymbol{r}_0\cdot\boldsymbol{F}(t_r) = \frac{1}{2}k_\perp^2 - \frac{F^2}{2}\frac{k_\perp^2+2I_p}{F^2-\boldsymbol{k}_\perp\cdot\dot{\boldsymbol{F}}} \\ &= \frac{-\boldsymbol{k}_\perp\cdot\dot{\boldsymbol{F}}(k_\perp^2+2I_p)}{2(F^2-\boldsymbol{k}_\perp\cdot\dot{\boldsymbol{F}})} - I_p.\end{aligned} \tag{B9}$$

For a circularly polarized laser pulse with an arbitrary envelope $f(t)$, the electric field is described as

$$\boldsymbol{F}(t) = F_0 f(t)[\sin(\omega_F t)\hat{\boldsymbol{e}}_x - \cos(\omega_F t)\hat{\boldsymbol{e}}_y], \tag{B10}$$

resulting in $-\boldsymbol{k}_\perp\cdot\dot{\boldsymbol{F}} = \omega_F F k_\perp$. Under this condition, the relation between the angular momentum [Eq. (B8)] and energy [Eq. (B9)] at the tunnel exit is always linear, expressed as

$$E = \omega_F L_z - I_p. \tag{6}$$

This is a general law whose slope is the frequency of the electric field. This suggests that the quantum underbarrier tunneling process is driven by the electric field of the light pulse.

Now, we look closely at the tunneling ionization probability W_{SPANE} as a function of $k_\perp$, from which we obtain the average initial transverse momentum $\langle k_\perp\rangle$. Substituting the electric field of the ultrashort laser pulses into Eq. (B6) yields

$$\langle k_\perp(t_r)\rangle \approx \frac{\omega_F I_p}{3F(t_r)}. \tag{B11}$$

This is consistent with the results of infinitely long circularly polarized laser pulses [31], when the carrier frequency of the electric field ω_F of the ultrashort pulse is used. This indicates that the transverse momentum distribution of the photoelectrons at the tunnel exit is determined by the electric field rather than the vector potential. Since tunneling ionization is a highly nonlinear process, the ionization rate depends exponentially on the electric-field strength. Therefore, we focus on the time instance $t_r = t_0$ corresponding to the laser field peak, so the peak position of the transverse momentum distribution is approximately

$$\langle k_\perp(t_0)\rangle \approx \frac{\omega_F I_p}{3F_0}. \tag{B12}$$

Since the asymptotic momentum $\boldsymbol{p}$ of the photoelectron relates to the initial momentum by $\boldsymbol{p} = \boldsymbol{k}_\perp - \boldsymbol{A}(t_r)$, where $\boldsymbol{k}_\perp$ and $\boldsymbol{A}(t_r)$ are antiparallel to each other, the peak position of the asymptotic momentum distribution is approximately

$$\langle p(t_0)\rangle \approx \langle k_\perp(t_0)\rangle + A_0 = \frac{\omega_F I_p}{3F_0} + A_0 = \frac{\omega_F I_p}{3F_0} + \frac{F_0}{\omega_A}. \tag{B13}$$

Note that $A_0 = F_0/\omega_A$, which is related to the carrier frequency of the vector potential.

To construct the dominant SAME in the asymptotic region, we focused solely on ionization that occurs at the peak of the laser pulse ($t_r = t_0$). For a N-cycle circularly polarized laser pulse, the vector potential is

$$\boldsymbol{A}(t) = A_0\cos^4\left(\frac{\omega_A t}{2N}\right)[\cos(\omega_A t)\hat{\boldsymbol{e}}_x + \sin(\omega_A t)\hat{\boldsymbol{e}}_y]. \tag{B14}$$

At the end of the laser field, the position is calculated by

$$\boldsymbol{r} = \int_{t_r=0}^{t_f} dt\{\boldsymbol{p}+\boldsymbol{A}(t)\} + \boldsymbol{r}_0 - \boldsymbol{\alpha}, \tag{B15}$$

where $t_f = N\pi/\omega_A$ and $\boldsymbol{\alpha} = (1/2)\int_{-t_f}^{t_f}\boldsymbol{A}(t)dt$. Therefore, the angular momentum at the end of the laser field is

$$\begin{aligned}L = \boldsymbol{r}\times\boldsymbol{p} &= \frac{\hat{\boldsymbol{e}}_z}{\omega_A}\left[\frac{A_0+k_\perp}{A_0+k_\perp\left(1+\frac{1}{N^2}\right)}\left(I_p+\frac{1}{2}k_\perp^2\right)\right. \\ &\quad \left.+\left(1+\frac{2N^2-5-3\cos(N\pi)}{2N^4-10N^2+8}\right)\left(A_0^2+A_0k_\perp\right)\right] \\ &= \frac{\hat{\boldsymbol{e}}_z}{\omega_A}\left[\frac{1}{\sqrt{U_p/E}+(1-\sqrt{U_p/E})\left(1+\frac{1}{N^2}\right)}(I_p+E_0)\right. \\ &\quad \left.+\left(1+\frac{2N^2-5-3\cos(N\pi)}{2N^4-10N^2+8}\right)(U_p+E-E_0)\right],\end{aligned} \tag{B16}$$

where E is the asymptotic energy and E_0 is the energy at the tunnel exit given by

$$\begin{aligned}E_0 &= \tfrac{1}{2}k_\perp^2 = \tfrac{1}{2}(p-A_0)^2 = \tfrac{1}{2}(\sqrt{2E}-\sqrt{2U_p})^2 \\ &= E(1-\sqrt{U_p/E})^2.\end{aligned} \tag{B17}$$

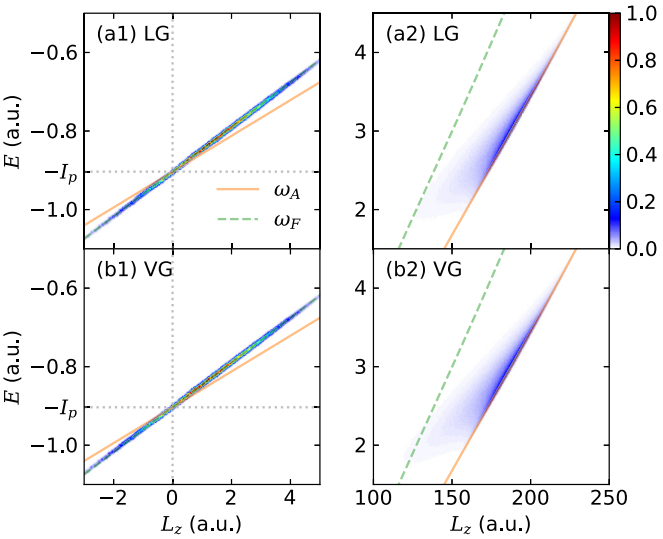

FIG. 9. Correlated spectra of angular momentum and energy (SAME) of photoelectrons (1) at the tunnel exit and (2) in the asymptotic region obtained using the SPANE method in both (a) length gauge (LG) and (b) velocity gauge (VG).

For the present ultrashort pulse with $N = 2$, Eq. (B16) is reduced to

$$L_z \overset{N\to 2}{=} \frac{1}{\omega_A}\left[\frac{4}{5-\sqrt{U_p/E}}(I_p+E_0)+\frac{4}{3}(U_p+E-E_0)\right], \tag{7}$$

where the frequency of the vector potential ω_A comes into play. These findings indicate that the dynamic behavior of photoelectrons in the asymptotic region is controlled by the vector potential instead of the electric field.

For infinitely long pulses with $N \to \infty$, Eq. (B16) is reduced to

$$L_z \overset{N\to\infty}{=} \frac{1}{\omega_A}(E+I_p+U_p), \tag{B18}$$

giving the SAME in the asymptotic region for long pulses

$$E = \omega_A L_z - I_p - U_p, \tag{B19}$$

where $\omega_A = \omega_F = \omega$ for infinitely long pulses.

APPENDIX C: GAUGE INVARIANCE

It is well established that it is preserved when the full Hamiltonian is used, as confirmed by TDSE simulations. This is also true for our study. To further verify the gauge invariance for the SPANE method, we have compared the results in both length gauge (LG) and velocity gauge (VG). In LG, the

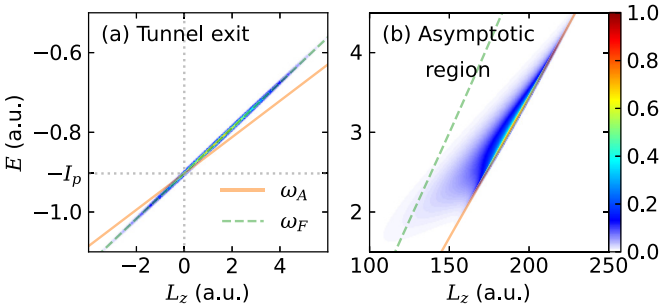

FIG. 10. Correlated spectra of angular momentum and energy (SAME) of photoelectrons (a) at the tunnel exit and (b) in the asymptotic region under the interaction of a three-dimensional model atom with the ultrashort laser pulse obtained using the SPANE method.

ionization amplitude is given by

$$M_{\boldsymbol{p}}^{\mathrm{LG}} = \sum_{t_s} \frac{\exp(iS_s)}{\{[\boldsymbol{p}+\boldsymbol{A}(t_s)]\cdot\boldsymbol{F}(t_s)\}^{\alpha/2}}, \tag{C1}$$

while, in VG, the ionization amplitude is

$$M_{\boldsymbol{p}}^{\mathrm{VG}} = \sum_{t_s} \frac{\exp(iS_s)}{\{[\boldsymbol{p}+\boldsymbol{A}(t_s)]\cdot\boldsymbol{F}(t_s)\}^{1/2}} \frac{\boldsymbol{p}\cdot\boldsymbol{A}(t_s)+A^2(t_s)/2}{(p^2+2I_p)^{\alpha}}. \tag{C2}$$

The phase is the same in both gauges:

$$S_s = -\int_{t_s}^{t_r}\left\{\frac{1}{2}[\boldsymbol{p}+\boldsymbol{A}(t)]^2+I_p\right\}dt. \tag{C3}$$

Using the SPANE method in both LG and VG, we have calculated the SAME of photoelectrons at the tunnel exit and in the asymptotic region. The results, shown in Fig. 9, demonstrate that both gauges yield nearly identical outcomes. This confirms the gauge invariance of our conclusions, which holds for both TDSE and SPANE calculations.

Therefore, our conclusion that tunneling dynamics are driven by the electric field, while the subsequent continuum motion is governed by the vector potential, remains valid regardless of the gauge choice. This implies that one cannot directly infer the effects of the electric field or vector potential on photoelectron dynamics from the interaction terms (i.e., $\boldsymbol{r}\cdot\boldsymbol{F}$ in LG and $\boldsymbol{p}\cdot\boldsymbol{A}+A^2/2$ in VG) in ultrashort laser pulses.

APPENDIX D: MODEL DIMENSIONALITY

The goal of the present work is to conceptually distinguish the roles of the electric field and vector potential in tunneling ionization dynamics. We demonstrate these roles using the minimal requirements of two dimensions for circular polarization. That said, we find it a good double check to perform a three-dimensional study, as shown in Fig. 10. The results demonstrate that our conclusions are independent of the dimensionality of the model.

[1] L. Vaidman, Role of potentials in the Aharonov-Bohm effect, Phys. Rev. A **86**, 040101(R) (2012).

[2] P. Pearle and A. Rizzi, Quantum-mechanical inclusion of the source in the Aharonov-Bohm effects, Phys. Rev. A **95**, 052123 (2017).

[3] C. Marletto and V. Vedral, Aharonov-Bohm phase is locally generated like all other quantum phases, Phys. Rev. Lett. **125**, 040401 (2020).

[4] X. Li, T. H. Hansson, and W. Ku, Gauge-independent description of the Aharonov-Bohm effect, Phys. Rev. A **106**, 032217 (2022).

[5] M. Uiberacker, T. Uphues, M. Schultze, A. J. Verhoef, V. Yakovlev, M. F. Kling, J. Rauschenberger, N. M. Kabachnik, H. Schröder, M. Lezius, K. L. Kompa, H.-G. Muller, M. J. J. Vrakking, S. Hendel, U. Kleineberg, U. Heinzmann, M. Drescher, and F. Krausz, Attosecond real-time observation of electron tunnelling in atoms, Nature (London) **446**, 627 (2007).

[6] E. Goulielmakis, Z.-H. Loh, A. Wirth, R. Santra, N. Rohringer, V. S. Yakovlev, S. Zherebtsov, T. Pfeifer, A. M. Azzeer, M. F. Kling, S. R. Leone, and F. Krausz, Real-time observation of valence electron motion, Nature (London) **466**, 739 (2010).

[7] Y. Ma, H. Ni, and J. Wu, Attosecond ionization time delays in strong-field physics, Chin. Phys. B **33**, 013201 (2024).

[8] C. I. Blaga, J. Xu, A. D. DiChiara, E. Sistrunk, K. Zhang, P. Agostini, T. A. Miller, L. F. DiMauro, and C. D. Lin, Imaging ultrafast molecular dynamics with laser-induced electron diffraction, Nature (London) **483**, 194 (2012).

[9] B. Wolter, M. G. Pullen, A.-T. Le, M. Baudisch, K. Doblhoff-Dier, A. Senftleben, M. Hemmer, C. D. Schröter, J. Ullrich, T. Pfeifer, R. Moshammer, S. Gräfe, O. Vendrell, C. D. Lin, and J. Biegert, Ultrafast electron diffraction imaging of bond breaking in di-ionized acetylene, Science **354**, 308 (2016).

[10] P. M. Kraus, B. Mignolet, D. Baykusheva, A. Rupenyan, L. Horný, E. F. Penka, G. Grassi, O. I. Tolstikhin, J. Schneider, F. Jensen, L. B. Madsen, A. D. Bandrauk, F. Remacle, and H. J. Wörner, Measurement and laser control of attosecond charge migration in ionized iodoacetylene, Science **350**, 790 (2015).

[11] M. Kübel, R. Siemering, C. Burger, N. G. Kling, H. Li, A. S. Alnaser, B. Bergues, S. Zherebtsov, A. M. Azzeer, I. Ben-Itzhak, R. Moshammer, R. de Vivie-Riedle, and M. F. Kling, Steering proton migration in hydrocarbons using intense few-cycle laser fields, Phys. Rev. Lett. **116**, 193001 (2016).

[12] L. Zhou, H. Ni, Z. Jiang, J. Qiang, W. Jiang, W. Zhang, P. Lu, J. Wen, K. Lin, M. Zhu, R. Dörner, and J. Wu, Ultrafast formation dynamics of D_3^+ from the light-driven bimolecular reaction of the D_2-D_2 dimer, Nat. Chem. **15**, 1229 (2023).

[13] H. Li, X. Gong, H. Ni, P. Lu, X. Luo, J. Wen, Y. Yang, X. Qian, Z. Sun, and J. Wu, Light-induced ultrafast molecular dynamics: From photochemistry to optochemistry, J. Phys. Chem. Lett. **13**, 5881 (2022).

[14] G. Paulus, F. Grasbon, H. Walther, P. Villoresi, M. Nisoli, S. Stagira, E. Priori, and S. De Silvestri, Absolute-phase phenomena in photoionization with few-cycle laser pulses, Nature (London) **414**, 182 (2001).

[15] M. F. Kling, C. Siedschlag, A. J. Verhoef, J. I. Khan, M. Schultze, T. Uphues, Y. Ni, M. Uiberacker, M. Drescher, F. Krausz, and M. J. J. Vrakking, Control of electron localization in molecular dissociation, Science **312**, 246 (2006).

[16] J. Venzke, T. Joyce, Z. Xue, A. Becker, and A. Jaron-Becker, Central frequency of few-cycle laser pulses in strong-field processes, Phys. Rev. A **98**, 063409 (2018).

[17] E. G. Neyra, P. Vaveliuk, E. Pisanty, A. S. Maxwell, M. Lewenstein, and M. F. Ciappina, Principal frequency of an ultrashort laser pulse, Phys. Rev. A **103**, 053124 (2021).

[18] Y. Ma, H. Ni, Y. Li, F. He, and J. Wu, Subcycle conservation law in strong-field ionization, Ultrafast Sci. **4**, 0071 (2024).

[19] J. Dubois, C. Lévêque, J. Caillat, R. Taïeb, U. Saalmann, and J.-M. Rost, Energy conservation law in strong-field photoionization by circularly polarized light, Phys. Rev. A **109**, 013112 (2024).

[20] M. Lein, E. K. U. Gross, and V. Engel, Intense-field double ionization of helium: Identifying the mechanism, Phys. Rev. Lett. **85**, 4707 (2000).

[21] X. M. Tong, K. Hino, and N. Toshima, Phase-dependent atomic ionization in few-cycle intense laser fields, Phys. Rev. A **74**, 031405(R) (2006).

[22] H. Ni, U. Saalmann, and J.-M. Rost, Tunneling ionization time resolved by backpropagation, Phys. Rev. Lett. **117**, 023002 (2016).

[23] H. Ni, U. Saalmann, and J.-M. Rost, Tunneling exit characteristics from classical backpropagation of an ionized electron wave packet, Phys. Rev. A **97**, 013426 (2018).

[24] H. Ni, N. Eicke, C. Ruiz, J. Cai, F. Oppermann, N. I. Shvetsov-Shilovski, and L.-W. Pi, Tunneling criteria and a nonadiabatic term for strong-field ionization, Phys. Rev. A **98**, 013411 (2018).

[25] C. Hofmann, A. Bray, W. Koch, H. Ni, and N. I. Shvetsov-Shilovski, Quantum battles in attoscience: Tunnelling, Eur. Phys. J. D **75**, 208 (2021).

[26] S. Eckart, Strong field-induced quantum dynamics in atoms and small molecules, J. Phys. B **57**, 202001 (2024).

[27] B. Feuerstein and U. Thumm, On the computation of momentum distributions within wavepacket propagation calculations, J. Phys. B **36**, 707 (2003).

[28] X. Wang, J. Tian, and J. H. Eberly, Extended virtual detector theory for strong-field atomic ionization, Phys. Rev. Lett. **110**, 243001 (2013).

[29] X. Wang, J. Tian, and J. Eberly, Virtual detector theory for strong-field atomic ionization, J. Phys. B **51**, 084002 (2018).

[30] R.-H. Xu and X. Wang, Extended virtual detector theory including quantum interferences, AIP Adv. **11**, 025124 (2021).

[31] H. Ni, S. Brennecke, X. Gao, P.-L. He, S. Donsa, I. Březinová, F. He, J. Wu, M. Lein, X.-M. Tong, and J. Burgdörfer, Theory of subcycle linear momentum transfer in strong-field tunneling ionization, Phys. Rev. Lett. **125**, 073202 (2020).

[32] Y. H. Kim, I. A. Ivanov, and K. T. Kim, Classical backpropagation for probing the backward rescattering time of a tunnel-ionized electron in an intense laser field, Phys. Rev. A **104**, 013116 (2021).

[33] M. Klaiber, Q. Z. Lv, S. Sukiasyan, D. Bakucz Canário, K. Z. Hatsagortsyan, and C. H. Keitel, Reconciling conflicting approaches for the tunneling time delay in strong field ionization, Phys. Rev. Lett. **129**, 203201 (2022).

[34] J.-P. Wang and F. He, Tunneling ionization of neon atoms carrying different orbital angular momenta in strong laser fields, Phys. Rev. A **95**, 043420 (2017).

[35] Q. Zhang, G. Basnayake, A. Winney, Y. F. Lin, D. Debrah, S. K. Lee, and W. Li, Orbital-resolved nonadiabatic tunneling ionization, Phys. Rev. A **96**, 023422 (2017).

[36] K. Liu, H. Ni, K. Renziehausen, J.-M. Rost, and I. Barth, Deformation of atomic $p_\pm$ orbitals in strong elliptically polarized laser fields: Ionization time drifts and spatial photoelectron separation, Phys. Rev. Lett. **121**, 203201 (2018).

[37] S. P. Goreslavski, G. G. Paulus, S. V. Popruzhenko, and N. I. Shvetsov-Shilovski, Coulomb asymmetry in above-threshold ionization, Phys. Rev. Lett. **93**, 233002 (2004).

[38] M. V. Frolov, N. L. Manakov, A. A. Minina, S. V. Popruzhenko, and A. F. Starace, Adiabatic-limit Coulomb factors for photoelectron and high-order-harmonic spectra, Phys. Rev. A **96**, 023406 (2017).

[39] Y. Ma, J. Zhou, P. Lu, H. Ni, and J. Wu, Influence of nonadiabatic, nondipole and quantum effects on the attoclock signal, J. Phys. B **54**, 144001 (2021).

[40] X. Mao, H. Ni, X. Gong, J. Burgdörfer, and J. Wu, Subcycle-resolved strong-field tunneling ionization: Identification of magnetic dipole and electric quadrupole effects, Phys. Rev. A **106**, 063105 (2022).

[41] S. V. Popruzhenko, Keldysh theory of strong field ionization: history, applications, difficulties and perspectives, J. Phys. B **47**, 204001 (2014).

[42] K. Amini, J. Biegert, F. Calegari, A. Chacón, M. F. Ciappina, A. Dauphin, D. K. Efimov, C. F. de Morisson Faria, K. Giergiel, P. Gniewek, A. S. Landsman, M. Lesiuk, M. Mandrysz, A. S. Maxwell, R. Moszyński, L. Ortmann, J. A. Pérez-Hernández, A. Picón, E. Pisanty, J. Prauzner-Bechcicki *et al.*, Symphony on strong field approximation, Rep. Prog. Phys. **82**, 116001 (2019).

[43] A. Nayak, M. Dumergue, S. Kühn, S. Mondal, T. Csizmadia, N. Harshitha, M. Füle, M. U. Kahaly, B. Farkas, B. Major, V. Szaszkó-Bogár, P. Földi, S. Majorosi, N. Tsatrafyllis, E. Skantzakis, L. Neoričić, M. Shirozhan, G. Vampa, K. Varjú, P. Tzallas *et al.*, Saddle point approaches in strong field physics and generation of attosecond pulses, Phys. Rep. **833**, 1 (2019).

[44] A. Jašarević, E. Hasović, R. Kopold, W. Becker, and D. Milošević, Application of the saddle-point method to strong-laser-field ionization, J. Phys. A **53**, 125201 (2020).